MATERIALS SCIENCE

Versatile acid solvents for pristine carbon nanotube assembly

Robert J. Headrick[1]†, Steven M. Williams[1]†, Crystal E. Owens[2], Lauren W. Taylor[1], Oliver S. Dewey[1], Cedric J. Ginestra[1], Lucy Liberman[3], Asia Matatyaho Ya'akobi[3], Yeshayahu Talmon[3], Benji Maruyama[4], Gareth H. McKinley[2], A. John Hart[2], Matteo Pasquali[1]*

Chlorosulfonic acid and oleum are ideal solvents for enabling the transformation of disordered carbon nanotubes (CNTs) into precise and highly functional morphologies. Currently, processing these solvents using extrusion techniques presents complications due to chemical compatibility, which constrain equipment and substrate material options. Here, we present a novel acid solvent system based on methanesulfonic or *p*-toluenesulfonic acids with low corrosivity, which form true solutions of CNTs at concentrations as high as 10 g/liter (≈0.7 volume %). The versatility of this solvent system is demonstrated by drop-in application to conventional manufacturing processes such as slot die coating, solution spinning continuous fibers, and 3D printing aerogels. Through continuous slot coating, we achieve state-of-the-art optoelectronic performance (83.6 %T and 14 ohm/sq) at industrially relevant production speeds. This work establishes practical and efficient means for scalable processing of CNT into advanced materials with properties suitable for a wide range of applications.

INTRODUCTION

Carbon nanotubes (CNTs) of varying quality and type are now manufactured at large scale (tens of kilograms per year to thousands of tons per year (*1*)), finding application in a diverse range of areas that capitalize on their electrical, thermal, and mechanical properties and may even contribute to decarbonizing the industrial sector (*2*, *3*). Of the commercialized CNT manufacturing technologies, floating catalyst chemical vapor deposition (CVD) processes produce the best combination of CNT quality and process scalability while yielding materials with apparently benign bio- and immune-compatibility profiles (*4*). For example, enhanced direct injection pyrolytic synthesis (eDIPs) (*5*) and plasma-enhanced CVD (PE-CVD) (*6*) yield highly crystalline CNTs in industrially relevant quantities (eDIPs is performed by Meijo Nanocarbon Ltd. at 2 tons/year, while PE-CVD by OCSiAl produces 75 tons/year) (*1*), albeit in disordered powder formats that require additional processing for application. Taking full advantage of CNT molecular properties requires assembly into well-defined structures with features that depend on the intended application (*7*). This can be accomplished with fluid phase assembly, which has been inspired by colloid and polymer processing methods such as aqueous dispersion (*8*), ionic dissolution (*9*), and superacid dissolution (*10*). In these processes, CNT macromolecules are suspended or dissolved in a liquid and subsequently reassembled into functional macroscopic structures depending on the desired application. Of these fluid processing technologies, superacids such as oleum and chlorosulfonic acid (CSA) have yielded the highest performing material properties because these acids directly dissolve CNT macromolecules without irreversible modification of their structures, leading to the formation of a liquid crystalline solution at high CNT concentration.

The properties of macroscopic CNT assemblies (films, fibers, etc.) produced via superacid processing vary systematically with CNT quality, suggesting that material performance will continue to improve as CNT manufacturing advances (*11*, *12*). However, these acids are highly corrosive, oxidative, and decompose reactively upon coagulation, introducing additional safety hazards, material compatibility barriers, and complicated solvent recovery. For example, additive manufacturing [three-dimensional (3D) printing] is an important application area in which the use of using superacids is particularly challenging. To date, 3D printing of neat, high-performance CNT materials has not succeeded because a sufficiently high concentration of individualized CNTs has not been attainable in solvents suitable for 3D printing processes. While superacids can yield sufficiently concentrated CNT solutions, they are incompatible with conventional processing equipment and commonly used plastics. This necessitates less aggressive solvents that can dissolve CNTs at high concentration without covalent damage.

Here, we introduce a versatile solvent system composed of anhydrous *p*-toluenesulfonic acid (*p*ToS) or methanesulfonic acid (MSA) mixed with a small amount of fuming sulfuric acid. The new acid solvents spontaneously dissolve CNTs to concentrations as high as 10 g/liter and yield thin films and fibers with electrical and mechanical properties on par with state-of-the-art technologies. We show that these acids can be used in die coating, screen printing, and injection molding with common substrates such as polyethylene terephthalate (PET) and polycarbonate, yielding high-quality CNT structures. We show that *p*ToS CNT solutions are particularly suitable for 3D printing via direct-write extrusion, as *p*ToS solidifies upon exposure to atmospheric moisture.

RESULTS

Dissolution of CNTs

Superacids such as oleum, CSA, and their mixtures protonate the CNT sidewall to form a polycarbocation without rehybridization of

[1]Department of Chemistry, Department of Chemical and Biomolecular Engineering, Department of Materials Science and NanoEngineering, The Smalley Institute for Nanoscale Science and Technology, and The Carbon Hub, Rice University, Houston, TX 77005, USA. [2]Department of Mechanical Engineering, Massachusetts Institute of Technology, Cambridge, MA 02139, USA. [3]Department of Chemical Engineering and the Russell Berrie Nanotechnology Institute (RBNI), Technion-Israel Institute of Technology, Haifa 3200003, Israel. [4]Air Force Research Laboratory, Materials and Manufacturing Directorate, WPAFB, OH 45387, USA.
*Corresponding author. Email: mp@rice.edu
†These authors contributed equally to this work.

the carbon atoms (*13*, *14*). The partial positive charge delocalizes along the length of the CNT and intercalates the bundle, causing adjacent CNTs to become repulsive and move into solution. At increasing concentration, CNTs form a biphasic mixture of isotropic and lyotropic liquid crystalline phases, eventually transitioning to a fully liquid crystalline phase beyond a critical concentration (*15*–*17*). The protonation strengths of anhydrous *p*ToS and MSA are insufficient for substantial CNT dissolution; however, we find that these acids can dilute CNT solutions in oleum, preserving CNT individualization while decreasing markedly the oxidative power of the overall solvent. For example, high-quality CNTs with diameters above ≈1.2 nm (see fig. S1) can be dissolved in ≈0.5 ml of oleum to form a CNT paste (10 mg/ml in fig. S2) and then diluted with 9.5 ml of *p*ToS or MSA (Fig. 1A). The CNTs are intercalated and debundled in the oleum dissolution step at concentrations up to 200 mg/ml [≈9 weight % (wt %)], forming a previously observed liquid crystalline morphology termed the "spaghetti phase" that is characterized by string-like structures of locally high concentrations of aligned CNTs in equilibrium with a low concentration isotropic phase (Fig. 1F) (*13*, *14*, *18*). At this stage, each CNT is fully encapsulated and positively charged by oleum. Dilution with *p*ToS or MSA separates the CNTs further while they retain enough positive surface charge to remain in solution. Notably, anhydrous *p*ToS is a solid at room temperature and melts above approximately 40°C, which provides major processing advantages because the solutions can be processed at moderate temperature and then solidified by cooling. Figure 1 (B to E) compares solutions at 0.5 mg/ml in different acid compositions imaged by transmitted light microscopy and polarized optical light microscopy (POM). The liquid crystalline morphology is transformed from spaghetti to a continuous bulk liquid crystalline phase that appears indistinguishable from what is obtained in pure CSA. The bulk liquid crystalline phase can be sustained at CNT concentrations as high as 10 mg/ml [0.66 wt %, ≈0.7 volume percent (volume %)] in 95 volume % MSA with 5 volume % oleum (Fig. 1G), which can be shear-aligned into a banded structure over long length scales (Fig. 1H). This dissolution strategy is simple and easily scalable, resulting in CNT solutions with a slightly red color due to the electron depletion from the CNTs to the acids (Fig. 1I). Direct addition of CNTs to a mixture of oleum and *p*ToS or MSA does not result in a homogeneous solution and appears black in color, indicating poor protonation of the CNTs (shown with visible absorbance in fig. S3). Similarly, adding the *p*ToS or MSA to the CNT paste too quickly can trap the system locally in the spaghetti phase, suggesting that these two states are both energy minima (fig. S4); in some cases, heating the samples to 60°C for >12 hours leads to a partial transition from the spaghetti phase state to the bulk liquid crystalline state.

Figure 2A shows cryogenic temperature scanning electron microscopy (cryo-SEM) and cryogenic temperature transmission electron microscopy (cryo-TEM) of a biphasic solution of CNTs dissolved in 95 volume % MSA and 5 volume % oleum at 0.5 mg/ml. The liquid crystalline domains observed by the POM are clearly visible as white/light gray structures in the cryo-SEM picture, surrounded by darker vitrified acid regions. Cryo-TEM indicates individualized CNTs within the acid, although the contrast between individual CNTs and vitrified MSA is relatively poor. To confirm individualization, dissolved CNTs were deposited onto a mica substrate for atomic force microscopy (AFM) analysis. An AFM image and corresponding height line scans are shown in Fig. 2B. Line scan s1 shows two individualized CNTs with diameters of approximately 1.3 nm, while scans s2 and s3 show two CNTs with diameters of 2.4 and 1.9 nm that overlap and cross each other. Achieving and maintaining CNT individualization in strong acids relies on the strength of the acid-CNT interaction, which can be quantified using resonant Raman spectroscopy. Electron depletion by the acid results in carbon-carbon bond stiffening and increases the energy of the tangential phonon mode, upshifting the G peak position proportionally (*19*, *20*). For HiPco CNTs (≈1-nm diameter CNTs produced by high-pressure carbon monoxide disproportionation) dissolved in CSA, the G peak position was shown to increase by 25 to 28 cm^{-1} (*14*, *15*). Figure 2C plots the G peaks resultant from 532-nm excitation for pristine CNTs in air, dissolved in pure oleum, and dissolved in 95 volume % MSA and 5 volume % oleum. Both acid solvents result in a G peak upshift of 26 cm^{-1}, suggesting that the strong interaction between the oleum and the CNTs remains intact after progressive dilution with MSA. Adding the CNTs directly to premixed 95 volume % MSA and 5 volume % oleum results in a G peak upshift of only 11 cm^{-1}, which is insufficient for CNT dissolution (see fig. S5 and table S1 for Raman spectra for additional acid combinations).

Because of the increased protonation afforded by this dissolution strategy, we produce inks at concentrations well above 0.5 mg/ml with phase behavior and rheological characteristics typical of true CNT solutions (*13*, *21*). Shear rheology of CNTs dissolved in MSA demonstrates continuously shear thinning behavior (Fig. 2D). The shear thinning index, *n*, can be calculated as $\eta = K\dot{\gamma}^{n-1}$, where η is the solution viscosity, $\dot{\gamma}$ is the shear rate, and *K* is the consistency index. In order of decreasing CNT concentration of 0.66, 0.33, and 0.15 wt % (10.0, 5.0, and 2.3 mg/ml), the solutions in MSA exhibit shear thinning indices, *n*, of 0.20, 0.29, and 0.36 (lower values of *n* correspond to stronger shear thinning behavior). This result is in good agreement with previous reports for CNTs dissolved in CSA, which exhibited shear thinning indices of 0.28 to 0.43 at concentrations ranging from 0.1 to 1.3 wt %, and indicates good processability of the solutions despite high CNT concentrations (*22*, *23*). An extended dataset and more detailed discussion about the rheological behavior of these solutions can be found in the Supplementary Materials (fig. S6).

High-performance CNT materials

The rheology and ambient processability of the CNT solutions facilitate their use for thin-film deposition and coating using commercially scalable techniques. In homogeneous film formation, film consolidation must be sufficiently fast to avoid dewetting from the substrate, which can be delayed by high solution viscosity and low surface tension and contact angle (*24*). In transparent electrodes, high performance is attained by evenly distributing individual or thin bundles of CNTs across the substrate; in fluid processing, this requires inks where CNTs are individualized. Figure 3A and movie S1 show continuous production of CNT transparent electrodes by roll-to-roll die coating. A syringe pump was used to meter the CNT-MSA solution onto a PET substrate that is fed into the die, which distributes the fluid into a thin film. The coated film was coagulated in-line by submersion into a warm water bath to remove the acid solvent and precipitate the CNTs onto the PET substrate. Figure 3B shows a photograph of a 90% transparent CNT film on PET, along with SEM of the mesh CNT network, which exhibits partial alignment in the coating direction and homogeneous coverage

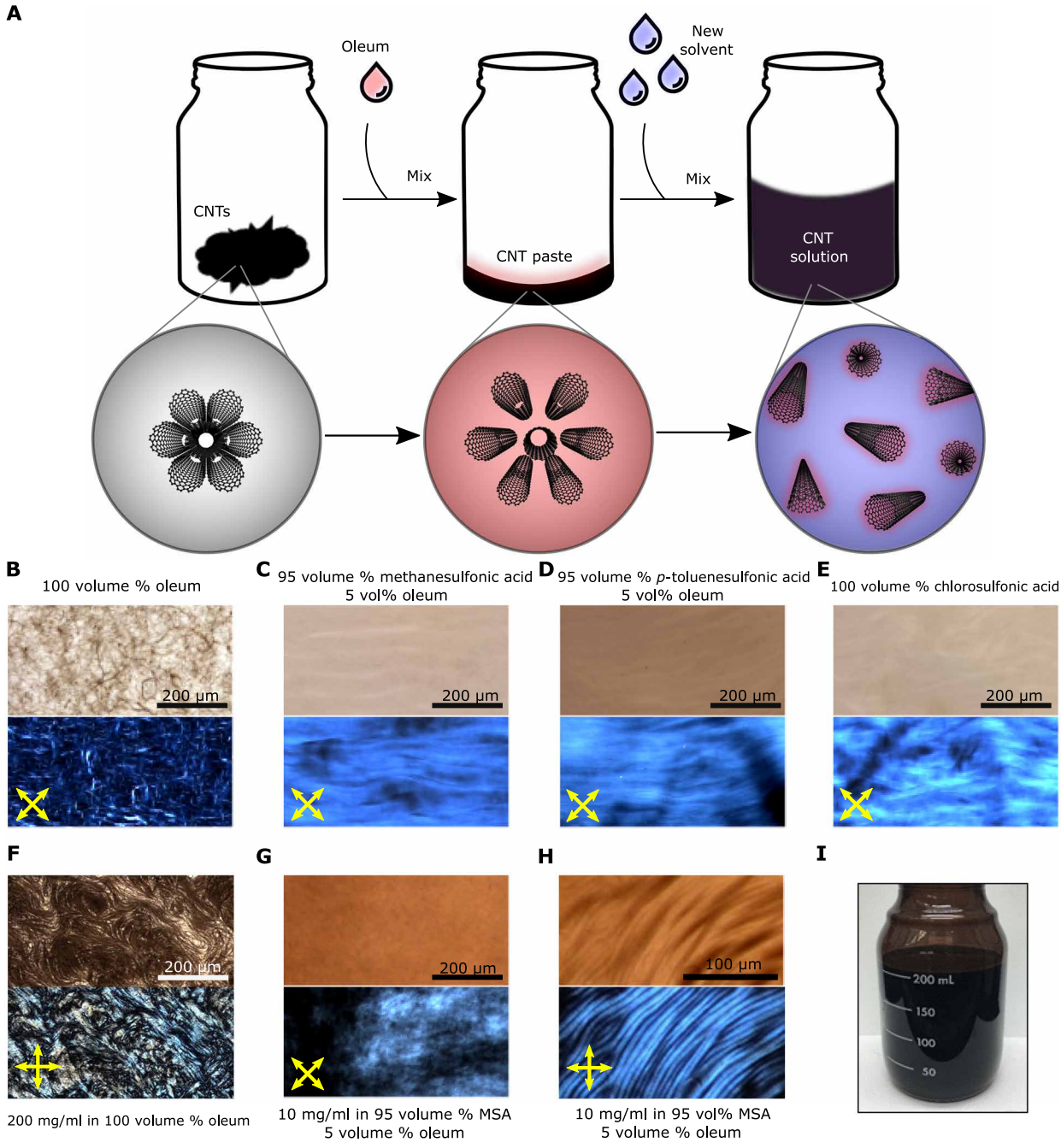

Fig. 1. Dissolution process and optical imaging of CNTs dissolved in various acids. (**A**) Dissolution strategy for preparing solutions of high-quality CNTs. Upon addition of oleum, CNTs become charged and separated, forming swollen strand-like structures. The diluting solvent then further separates the individual CNTs from each other. (**B** to **H**) Transmitted light (top half) and cross-polarized microscopy (bottom half) images of (B) spaghetti phase in 100 volume % oleum and bulk liquid crystalline solutions in (C) 95 volume % MSA and (D) *p*ToS mixed with 5 volume % oleum, (E) pure CSA, (F) liquid crystalline paste (200 mg/ml) in pure oleum before dilution, (G) CNTs (10 mg/ml) in 95 volume % MSA with 5 volume % oleum, displaying bulk liquid crystalline behavior and (H) shear banding induced after sliding the bulk liquid crystalline solution between glass slide and coverslip. (**I**) Two hundred milliliters of 0.5 mg/ml CNTs dissolved in 95 volume % *p*ToS with 5 volume % oleum, demonstrating the scalable nature of the dissolution strategy.

of small bundles. To simplify comparison of optoelectronic performance, we define a transparent electrode figure of merit (FOM) as the following (*25*)

$$\frac{\sigma_{dc}}{\sigma_{op}} = \frac{Z_0}{2R_s(T^{-0.5} - 1)}$$

where R_s is the sheet resistance in ohm per square, T is the transmittance, and $Z_0 \approx 376.73$ ohm is the characteristic impedance of vacuum. In this case, high values of FOM indicate higher performance films. Transparent electrodes produced by this method have excellent optoelectronic properties over long lengths. Position-dependent

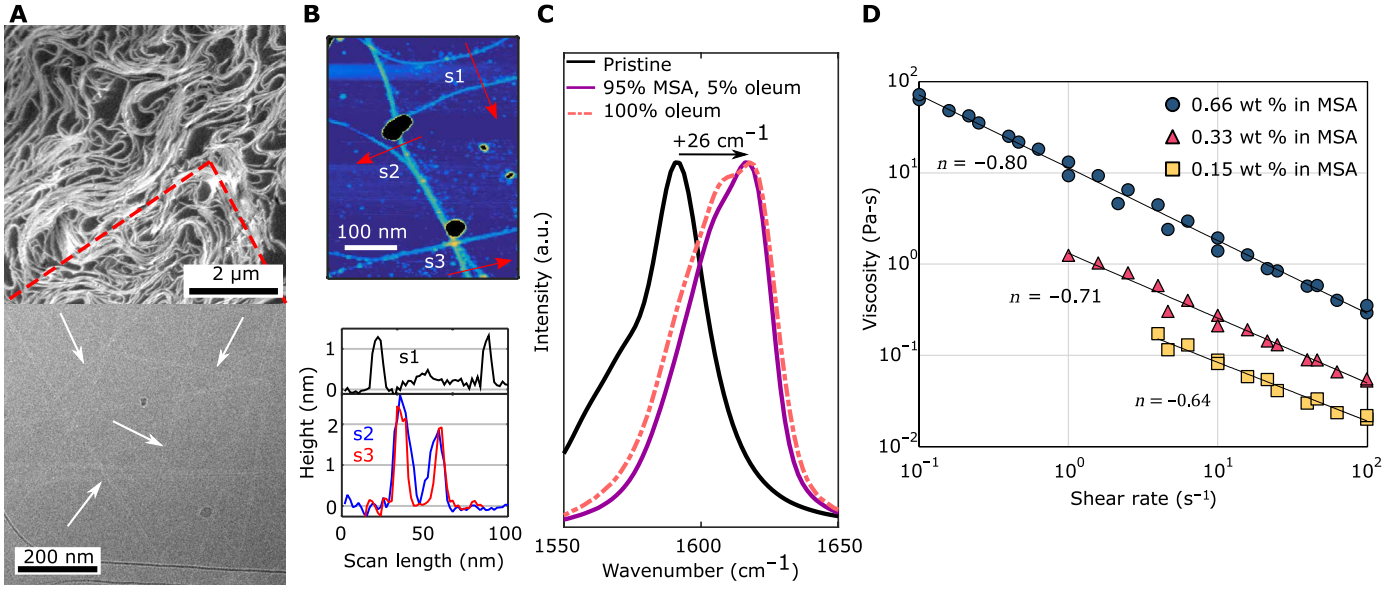

Fig. 2. Strong acid-CNT interaction yields individualization. (**A**) Cryo-SEM (top) and cryo-TEM (bottom) micrographs of CNTs dissolved in 95 volume % MSA with 5 volume % oleum at 0.5 and 0.05 mg/ml, respectively, showing locally aligned liquid crystalline domains and individualized CNTs. (**B**) AFM image of CNT deposited from dilute MSA solution (top) height profile scans (bottom). Line scans reveal individual CNTs with diameters of approximately 1.3, 1.9, and 2.4 nm. (**C**) Raman spectra of the G peak region of pristine CNTs (in air) and dissolved in acids. a.u., arbitrary units. (**D**) Shear thinning rheological behavior of CNTs dissolved in 95 volume % MSA with 5 volume % oleum at 2.3, 5, and 10 mg/ml. Each sample was tested twice to verify solution stability. The shear thinning index, *n*, for each curve is indicated.

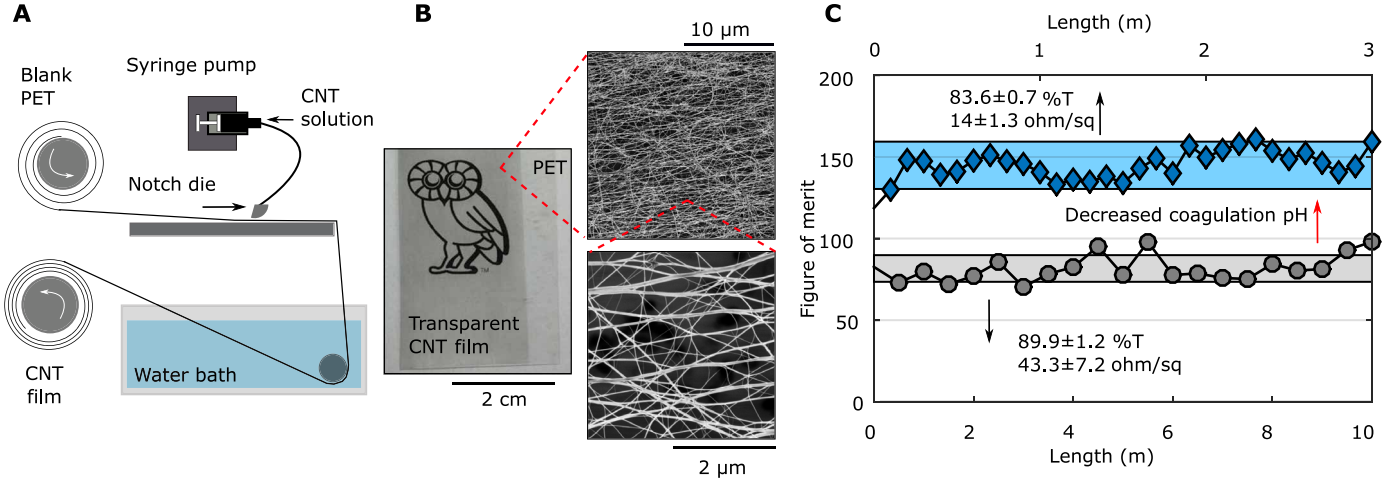

Fig. 3. Continuous production of high-performance CNT electrodes. (**A**) Schematic detailing the die coating setup. (**B**) Picture and SEM of a typical transparent CNT film produced by this method. CNT bundles form a sparse but homogeneous web-like sheet over the substrate with partial alignment in the coating direction. (**C**) FOM along the length of continuously produced CNT films (deposited from 95 volume % MSA with 5 volume % oleum) demonstrating the low variability of film transparency and conductivity.

FOMs for two different CNT films coated at 0.5 m/min are plotted in Fig. 3C over 3 and 10 m. We achieve average FOMs of 80 (89.9 %T and 43.3 ohm/sq) and 143 (83.6 %T and 14 ohm/sq) for the two films, substantially higher than what is achieved for CNTs of similar quality when filtered (FOM ≈ 64.3) (*26*) or shear aligned (FOM ≈ 58) from CSA (*27*). An FOM of 143 is the highest reported optoelectronic performance for neat CNT films to date (i.e., films whose optoelectronic properties are primarily due to the CNTs), outperforming flexible indium tin oxide (FOM ≈ 116) and equivalent to CNT films prepared by floating catalyst-CVD (FOM ≈ 139), here at a mass-throughput deposition rate that is ≈70× higher (*28*). Additional discussion and sheet resistance versus transparency plots to compare performance and production rates of different CNT thin-film production methods (*22*, *24*, *26*, *28*, *29*), graphene (*30*), and batches of CNTs can be found in fig. S7. Note that, to date, no continuous production of graphene or graphene oxide films has achieved performance better than 200 ohm/sq and 75 %T (*31*). Both films show little variability in transmittance (≈1 %T), confirming consistent CNT deposition rates and film thickness along the entire length of the coated PET. Nearly all of the variability in the FOM results from changes in the sheet resistance, which is likely due to suboptimal control over coagulation, leading to variability in bundle

morphology at micrometer-length scales and small changes in the amount of doping from residual acid. Despite the partial alignment observed in the SEM, the films exhibit isotropic electrical conductivity over 1 mm lengths (fig. S8); anisotropic electrical conductivity in aligned CNT films becomes prevalent at centimeter-length scales, particularly for dedoped films (*27*). The primary difference between the production processes for the two films is the temperature and pH of the coagulation bath. The higher-performance film was produced at a slightly lower temperature (≈60°C) and pH (accumulated during film production), both of which slow coagulation.

This solvent system is compatible with multiple batches of high-quality CNTs from different manufacturers, which affect thin-film performance (fig. S7). The transparency and sheet resistance of films produced from MSA and *p*ToS solutions proved to be stable while stored in open air (fig. S9). These properties were achieved with commonly used coating equipment and substrates in ambient air. Moreover, MSA and *p*ToS do not decompose upon coagulation in water and can be recycled in the process, substantially lowering environmental impact and energy and processing costs relative to pure superacid processing. At current CNT and acid pricing, material costs for producing 90 %T films are below $10/m^2—additional discussion and the impact of CNT cost and coating concentration can be found in fig. S10.

Stable liquid crystalline solutions make possible the continuous production of CNT fibers through similar techniques. A syringe pump was used to meter CNT-MSA solution through a stainless steel needle submerged in a water coagulation bath, and the solidified CNT fiber was collected on a continuously winding drum (Fig. 4A). The acid solvent diffuses into the water bath, causing the CNTs to precipitate in the form of a cylindrical fiber with substantial axial alignment (Fig. 4B and movie S2). Representative stress-strain curves from CNT fibers produced from MSA are shown in Fig. 4C; the stress-strain behavior closely resembles that of CNT fibers produced by solid state processing and spinning from CSA. We achieve a tensile strength of 1.11 GPa (0.78 N/tex) and an electrical conductivity of 5.2 MS/m (3500 S-m^2/kg). These properties are ≈50% of what is reported for solution spinning of similar quality CNTs from CSA (2.4 GPa and 8.5 MS/m) and will likely improve with further processing optimization, which is known to play a critical role in fiber performance (*11*). The volumetric density of these fibers is 1.49 g/cm^3, which is lower than what has been measured for optimally densified fibers (<1.60 g/cm^3), indicating that properties can be improved by increasing packing density within the internal fiber structure (*27*).

The unique properties of *p*ToS solidification combined with the shear thinning nature of the CNT solutions allow us to fabricate self-supporting 3D structures with custom shapes using 3D printing in ambient conditions (movie S3). We configured two commercially available 3D printers to print *p*ToS by replacing the polymer extrusion nozzles with fine needles, which are fed with CNT solution using syringe pumps (Fig. 5). Using a resistive heater, the nozzle can be heated to 50° to 70°C to hold the *p*ToS in a liquid state. Upon extrusion from the nozzle, the surface layer of the *p*ToS reacts with ambient moisture to form a skin of solid *p*ToS monohydrate (melting point 106°C). This acts as a solid support during subsequent printing of additional layers and is reminiscent of the oxide layer that has enabled 3D printing of a liquid metal mixture (*32*). Using a micrometer stage-based extruder, we obtain fine control over liquid extrusion into highly controlled structures, as demonstrated by the 2D pattern printed onto a polyetherimide substrate in Fig. 5B (movie S4). Well-defined 3D structures such as the cylinder in Fig. 5C are easily obtained by printing additional layers (movie S5).

After printing, the acid solvent is readily removed by submersion in a nearby coagulant bath (such as water, ethanol, acetone, or isopropanol). The resulting structure can then be freeze-dried to leave a self-supporting aerogel composed of pristine CNTs that retains the printed shape. An annotated SEM micrograph of a printed log pile CNT aerogel is shown in Fig. 5D, in which extruded filaments of a lower layer (red arrows) are merged with an orthogonally extruded filament of the next layer (yellow arrow), demonstrating intimate contact between printed layers. This alternating, cross-ply architecture results in submillimeter voids between printed filaments, as indicated by white arrowheads in the micrograph. The interiors of the individual printed filaments consist of smaller pores (≈5 μm) separated by thin sheets of bundled CNTs (Fig. 5E), providing a percolated network of CNTs for electrical conduction and mechanical strength. Despite their high porosity (corresponding to a density of only 18 mg/cm^3), the printed aerogels retain high conductivities of

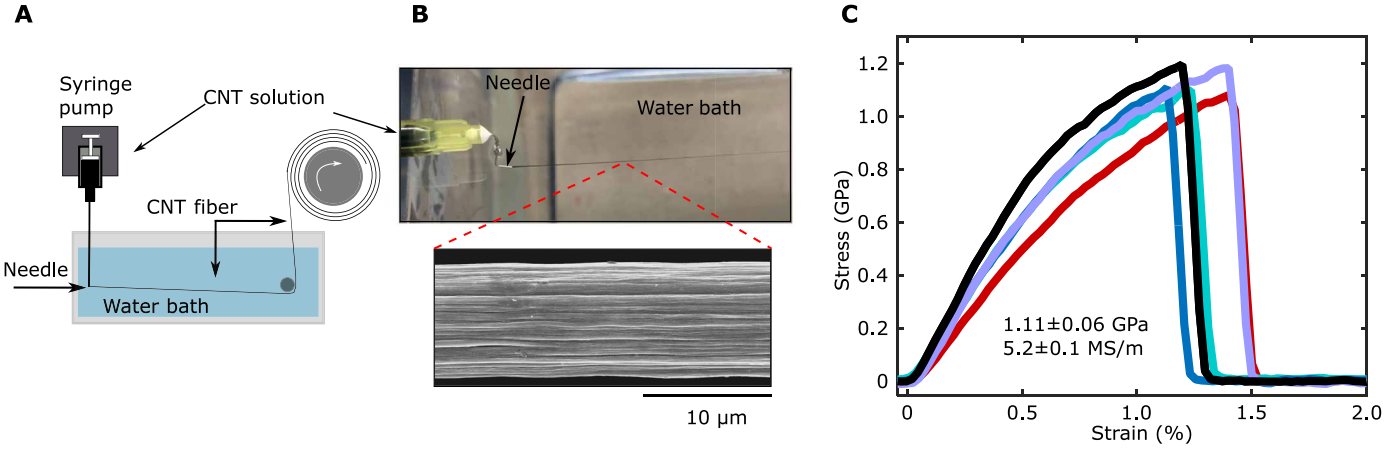

Fig. 4. Solution spinning CNT fiber. (**A**) Schematic of CNT fiber spinning setup. (**B**) Solution spinning close-up and fiber morphology SEM showing the well-aligned and cylindrical structure of the solution-spun CNT fiber produced from 95 volume % MSA with 5 volume % oleum. (**C**) Representative stress-strain curves from CNT fibers produced from CNT-MSA solution.

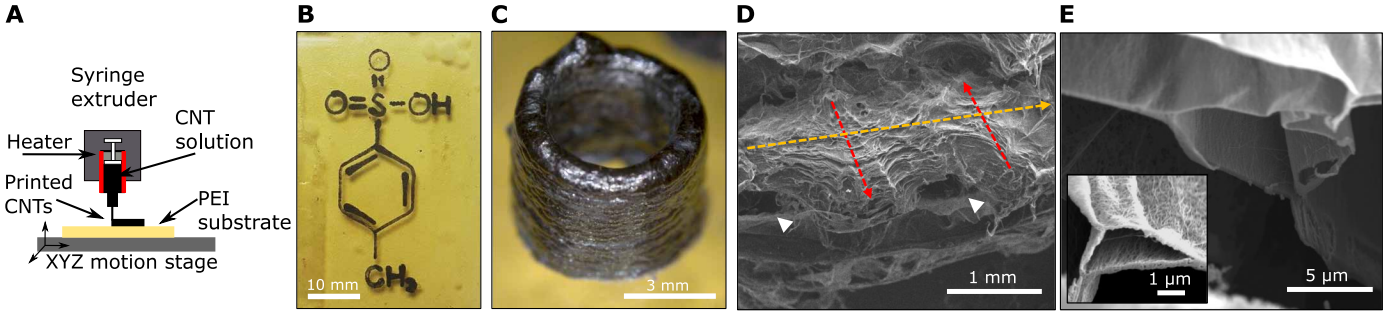

Fig. 5. 2D and 3D printing of CNT structures. (**A**) Schematic of 3D printing of CNT dissolved in 95 volume % *p*ToS with 5 volume % oleum. (**B**) 2D direct write printed pattern of CNTs depicting the molecular structure of *p*ToS on polyamide. (**C**) 3D-printed cylinder before coagulation. (**D**) SEM of a 3D-printed CNT log pile after coagulation, demonstrating the strong interlayer adhesion. Red and yellow arrows represent orthogonal print lines that have merged, and white arrowheads represent pores between print lines. (**E**) Focused ion beam cut cross section of a single print layer showing the porous aerogel structure.

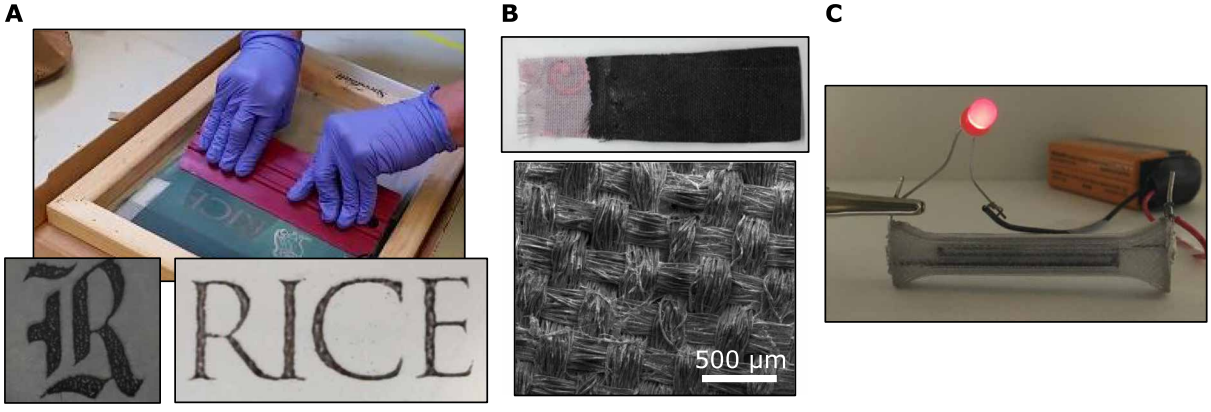

Fig. 6. Application of CNT inks to various substrates. (**A**) Screen printing, (**B**) coated polyester fabric, and (**C**) polycarbonate block with porous serpentine wire that are electrically conductive.

800 S/m due to the long, pristine CNTs that compose the main structure and residual acid doping. This equals a specific conductivity of 44 S-m^2/kg, which can be improved to 55 S-m^2/kg by collapsing with capillary densification, yielding a specific conductivity comparable to laser-sintered graphene foams (58 S-m^2/kg) (*33*). Use of industrial-grade 3D printers should enable even greater feature fidelity than the printers used in this study.

We further explore the enhanced material compatibility of *p*ToS solutions in Fig. 6A by patterning CNTs onto a Teflon/glass composite and PET substrates by benchtop silk-screen printing, followed by coagulation in acetone. The silk-screen and photo-emulsion mask remain undamaged after multiple coating applications followed by cleaning with isopropyl alcohol. As is common in screen printing, resolution is limited by the screen mesh and mask. Figure 6B shows a picture and SEM of fabric that has been coated with CNTs, which remains intact after coagulation and drying, rendering the fabric electrically conductive with a low resistance (30 ohm/cm). We also inject the ink directly into a hollow channel of a polycarbonate block, which results in a porous and conductive (2 ohm/cm) trace after coagulation (Fig. 6C). Using this dissolution strategy enables advanced device design for smart textiles and injectable wiring or electrodes with CNTs that are of substantially higher quality and purity than what has been achieved through aqueous and organic processing methods.

DISCUSSION

Strong acids have been used as solvents for dissolution and processing of rodlike aramid polymers since the 1970s (*34*). Until now, acid solutions of CNTs have been limited to superacid-strength solvents. The new acid solvent systems based on MSA or *p*ToS combined with oleum produce stable CNT solutions at high mass concentration (demonstrated up to 0.66 wt %), with individualized CNTs organized in a bulk liquid crystalline phase, while avoiding CSA's reactivity and oxidizing power. We have demonstrated novel acid-based CNT solutions that enable previously unfeasible production methods such as roll-to-roll coating and 3D printing. Continuously coated transparent electrodes on PET provide optoelectronic performance that is suitable for liquid crystal display (LCD) and touch screen applications (<500 ohm/sq at 90 %T), on-par with indium tin oxide (50 ohm/sq at 90 %T) (*30*), and outperform in terms of properties and manufacturing rates all transparent CNT films reported to date. This solvent system is compatible with multiple batches of high-quality CNTs from different manufacturers, which affect thin-film performance (fig. S7). CNT fibers are produced with competitive properties that are likely to improve with additional process optimization while also allowing for simpler solvent recycling, which will reduce manufacturing costs substantially. Last, CNTs can be deposited onto relatively sensitive materials (polyester fabric, polycarbonate, and silk screen) with no evidence of material degradation. In this work,

thin-film coating, fiber spinning, 3D printing, and screen printing were all performed on unventilated benchtops as these inks have sufficiently low vapor pressure and do not produce dangerous fumes at room temperature or during coagulation. These inks enable a wide range of processing technologies inaccessible to pure superacid solvents while yielding mechanical and electrical properties suitable for next-generation device integration.

MATERIALS AND METHODS

Material preparation

Oleum (20 wt % excess SO_3 fuming sulfuric acid), CSA, MSA, and *p*ToS monohydrate were purchased from Sigma-Aldrich. As-produced CNTs were purchased from Meijo Nano Carbon Co. Ltd. with an average diameter of 2.3 nm (batch EC2.0) or 1.5 nm (batch EC1.5) and OCSiAl (Tuball) and purified by furnace oxidation at 400°C with 80 sccm of N_2 and 20 sccm of O_2 for 12 hours to remove amorphous carbon (≈4% mass loss) and enable the CNTS to dissolve into acid solvents (fig. S1 for Raman spectra confirming diameters and quality of Meijo CNTs). The purification process takes advantage of the increased reactivity of sp^3 hybridized (amorphous) carbon relative to sp^2 hybridized carbon—there is no evidence to suggest that the CNT sidewalls are oxidized or that oxygen functional groups improve dissolution into strong acids. All experiments were performed with EC1.5 except for the 3D printing, which used EC2.0. *p*ToS monohydrate was dried by heating to 110°C under vacuum in a round-bottom flask until bubble formation ceased, leaving a colorless to lightly rose-colored liquid. CNT-MSA and CNT-*p*ToS solutions were prepared by addition of CNTs to 0.5 ml of oleum and speed-mixed using a FlakTek mixer for 10 min. The sample was then diluted by addition of 9.5 ml of MSA (or anhydrous *p*ToS melted by heat gun to above 40°C) and mixed again. Dry CNT materials were recovered from acid solvents by precipitating in acetone, rinsing with water until neutral, and freeze drying.

Processing and characterization

The viscosity average aspect ratio after purification was estimated by dissolving the CNT sample in CSA and measuring the extensional viscosity by capillary breakup extensional rheometry (*16*). Transmitted and polarized light microscopy was performed using a Zeiss Axioplan II. Raman spectroscopy was performed on solid samples with a Renishaw InVia confocal microscope with excitation wavelengths of 785, 633, and 532 nm to evaluate CNT crystallinity after purification. Raman measurements (532 nm) and transmitted light images (Zeiss Axioplan) on CNTs dissolved in acids were collected with the sample sandwiched between glass slide and coverslip or inside a flame-sealed glass 100-μm capillary. Shear rheology was performed with a TA Instruments ARES G2 rheometer using cone and plate geometry at 100°C on a CNT-MSA solution of MEC2.0 at 2.3, 5, and 10 mg/ml under a flow of dry air. Cryo-TEM of CNTs dissolved in 95 volume % MSA with 5 volume % oleum was performed by a Thermo Fisher Scientific (FEI) Talos 200C high-resolution TEM, using a Gatan 626 cryo-holder to maintain the cryo-specimens below −175°C in the microscope. Images were recorded digitally by an FEI Falcon III direct-imaging camera, using the low-dose imaging mode to reduce electron-beam radiation damage. Cryo-SEM was performed by a Zeiss Ultra Plus HR-SEM equipped with a Leica VT100 cold-stage system to maintain the cryo-specimens below −143°C in the microscope. Cryo-TEM and cryo-SEM specimens were prepared in a controlled environment vitrification system and were vitrified by plunging into liquid nitrogen. For cryo-TEM specimens, a drop was applied onto a perforated carbon film supported on a 3-mm copper TEM grid. The drop was blotted with a filter paper to form a thin film (<300 nm). Cryo-SEM specimens were prepared by immersing a 3-mm copper TEM grid in a solution and placing it between two gold planchettes. The specimens were vitrified in liquid nitrogen and freeze-fractured in a BAF060 unit (Leica AG, Liechtenstein) at −167°C. AFM samples were prepared from <1 part per million of MSA solution evaporated onto Mica at 420°C and then washed with deionized water and acetone. The sample was then dried at 200°C for 1 hour. AFM scans were obtained with a Park NX20 AFM in tapping mode at a line scan rate of 1 Hz.

Continuous production of transparent CNT electrodes was performed using a custom notch-die coating setup. A syringe pump was used to meter the CNT-MSA solution onto a moving PET substrate that fed into the notch die, distributing the fluid into a thin film. The coated thin film was then coagulated in-line with a warm water bath and collected on a winding drum. The water was allowed to cool over time, and the pH decreased as the water was not replenished. Thin-film sheet resistance was measured with a on a Jandel RM3-AR linear four-point probe, while transmittance was measured at 550 nm using a Shimadzu UV-1800 spectrometer with the films on the substrates where they were coated. The reported transparency values have the absorbance of the appropriate substrate subtracted and represent only the transparency of the CNT film, which is consistent with the methods in comparative literature values reported here. Scanning electron micrographs of transparent electrodes were obtained with an FEI Quanta 400 ESEM FEG or an FEI Helios Nanolab 660 SEM/FIB; films were transferred onto copper grids and then attached to carbon tape on aluminum stubs for imaging.

Solution spinning of CNT fiber was accomplished through extrusion of CNT-MSA solution through a stainless-steel needle (30-gauge blunt tip) submerged in a hot water coagulation bath. Note that the CNT solution was flowing from the syringe and exiting through a needle submerged in a coagulation bath—under sufficient flow, the coagulation process is not fast enough for water to travel up the needle. The solidified CNT fiber was collected on a continuously winding drum. CNT fiber tensile breaking tests and linear density were determined simultaneously using a vibroscopic measurement described previously (*35*). CNT fiber conductivity was measured using a custom built four-point probe with an inner electrode distance of 7 cm connected to an HP 34401A multimeter.

3D printing was performed using two different setups, the first using a Lulzbot TAZ 6 3D printer with custom syringe pump (*36*) assembly as printhead. The solution was extruded from a BD syringe through attached 21-gauge Luer-Lock syringe tip. In the second setup, a Makergear M2 was modified to have a custom syringe pump assembly as the printhead and equipped with a resistive heater on the extrusion needle to control the extrudate temperature to be between 50° and 90°C as desired (*37*). The ink was extruded from a Global brand 1-ml syringe using a variety of Luer-lock needle sizes from 20 to 32 gauge. Machine Gcode was generated by custom code. As-printed CNT acid structures were washed with multiple deionized water baths and freeze-dried for 24 hours, resulting in free-standing CNT aerogels. Screen printing was performed with a screen and photo-emulsion mask purchased from Speedball.

SUPPLEMENTARY MATERIALS

Supplementary material for this article is available at https://science.org/doi/10.1126/sciadv.abm3285

REFERENCES AND NOTES

1. L. Zheng, J. Attwood, Advanced Materials Primer: Carbon Nanotubes. (BloombergNEF, 2021).
2. R. Rao, C. L. Pint, A. E. Islam, R. S. Weatherup, S. Hofmann, E. R. Meshot, F. Wu, C. Zhou, N. Dee, P. B. Amama, J. Carpena-Nuñez, W. Shi, D. L. Plata, E. S. Penev, B. I. Yakobson, P. B. Balbuena, C. Bichara, D. N. Futaba, S. Noda, H. Shin, K. S. Kim, B. Simard, F. Mirri, M. Pasquali, F. Fornasiero, E. I. Kauppinen, M. Arnold, B. A. Cola, P. Nikolaev, S. Arepalli, H.-M. Cheng, D. N. Zakharov, E. A. Stach, J. Zhang, F. Wei, M. Terrones, D. B. Geohegan, B. Maruyama, S. Maruyama, Y. Li, W. W. Adams, A. J. Hart, Carbon nanotubes and related nanomaterials: Critical advances and challenges for synthesis toward mainstream commercial applications. *ACS Nano* **12**, 11756–11784 (2018).
3. M. Pasquali, C. Mesters, Opinion: We can use carbon to decarbonize—and get hydrogen for free. *PNAS*. **118**, e2112089118 (2021).
4. J. S. Yan, M. Orecchioni, F. Vitale, J. A. Coco, G. Duret, S. Antonucci, S. S. Pamulapati, L. W. Taylor, O. S. Dewey, M. Di Sante, A. M. Segura, C. Gurcan, F. Di Lisa, A. Yilmazer, M. D. McCauley, J. T. Robinson, M. Razavi, K. Ley, L. G. Delogu, M. Pasquali, Biocompatibility studies of macroscopic fibers made from carbon nanotubes: Implications for carbon nanotube macrostructures in biomedical applications. *Carbon.* **173**, 462–476 (2021).
5. T. Saito, S. Ohshima, T. Okazaki, S. Ohmori, M. Yumura, S. Iijima, Selective diameter control of single-walled carbon nanotubes in the gas-phase synthesis. *J. Nanosci. Nanotechnol.* **8**, 6153–6157 (2008).
6. M. R. Predtechensky, O. M. Tukhto, I. Y. Koval, System and method for producing carbon nanotubes U.S. Patent 8551413 (2013).
7. M. F. L. D. Volder, S. H. Tawfick, R. H. Baughman, A. J. Hart, Carbon nanotubes: Present and future commercial applications. *Science* **339**, 535–539 (2013).
8. B. Vigolo, A. Pénicaud, C. Coulon, C. Sauder, R. Pailler, C. Journet, P. Bernier, P. Poulin, Macroscopic fibers and ribbons of oriented carbon nanotubes. *Science* **290**, 1331–1334 (2000).
9. A. Pénicaud, P. Poulin, A. Derré, E. Anglaret, P. Petit, Spontaneous dissolution of a single-wall carbon nanotube salt. *J. Am. Chem. Soc.* **127**, 8–9 (2005).
10. L. M. Ericson, H. Fan, H. Peng, V. A. Davis, W. Zhou, J. Sulpizio, Y. Wang, R. Booker, J. Vavro, C. Guthy, A. N. G. Parra-Vasquez, M. J. Kim, S. Ramesh, R. K. Saini, C. Kittrell, G. Lavin, H. Schmidt, W. W. Adams, W. E. Billups, M. Pasquali, W.-F. Hwang, R. H. Hauge, J. E. Fischer, R. E. Smalley, Macroscopic, neat, single-walled carbon nanotube fibers, single-walled carbon nanotube fibers. *Science* **305**, 1447–1450 (2004).
11. D. E. Tsentalovich, R. J. Headrick, F. Mirri, J. Hao, N. Behabtu, C. C. Young, M. Pasquali, Influence of carbon nanotube characteristics on macroscopic fiber properties. *ACS Appl. Mater. Interfaces* **9**, 36189–36198 (2017).
12. L. W. Taylor, O. S. Dewey, R. J. Headrick, N. Komatsu, N. M. Peraca, G. Wehmeyer, J. Kono, M. Pasquali, Improved properties, increased production, and the path to broad adoption of carbon nanotube fibers. *Carbon* **171**, 689–694 (2021).
13. V. A. Davis, L. M. Ericson, A. N. G. Parra-Vasquez, H. Fan, Y. Wang, V. Prieto, J. A. Longoria, S. Ramesh, R. K. Saini, C. Kittrell, W. E. Billups, W. W. Adams, R. H. Hauge, R. E. Smalley, M. Pasquali, Phase behavior and rheology of SWNTs in superacids. *Macromolecules* **37**, 154–160 (2004).
14. S. Ramesh, L. M. Ericson, V. A. Davis, R. K. Saini, C. Kittrell, M. Pasquali, W. E. Billups, W. W. Adams, R. H. Hauge, R. E. Smalley, Dissolution of pristine single walled carbon nanotubes in superacids by direct protonation. *J. Phys. Chem. B* **108**, 8794–8798 (2004).
15. V. A. Davis, A. N. G. Parra-Vasquez, M. J. Green, P. K. Rai, N. Behabtu, V. Prieto, R. D. Booker, J. Schmidt, E. Kesselman, W. Zhou, H. Fan, W. W. Adams, R. H. Hauge, J. E. Fischer, Y. Cohen, Y. Talmon, R. E. Smalley, M. Pasquali, True solutions of single-walled carbon nanotubes for assembly into macroscopic materials. *Nat Nano.* **4**, 830–834 (2009).
16. D. E. Tsentalovich, A. W. K. Ma, J. A. Lee, N. Behabtu, E. A. Bengio, A. Choi, J. Hao, Y. Luo, R. J. Headrick, M. J. Green, Y. Talmon, M. Pasquali, Relationship of extensional viscosity and liquid crystalline transition to length distribution in carbon nanotube solutions. *Macromolecules* **49**, 681–689 (2016).
17. O. Kleinerman, L. Liberman, N. Behabtu, M. Pasquali, Y. Cohen, Y. Talmon, Direct imaging of carbon nanotube liquid-crystalline phase development in true solutions. *Langmuir* **33**, 4011–4018 (2017).
18. P. K. Rai, R. A. Pinnick, A. N. G. Parra-Vasquez, V. A. Davis, H. K. Schmidt, R. H. Hauge, R. E. Smalley, M. Pasquali, Isotropic–Nematic phase transition of single-walled carbon nanotubes in strong acids. *J. Am. Chem. Soc.* **128**, 591–595 (2006).
19. G. U. Sumanasekera, J. L. Allen, S. L. Fang, A. L. Loper, A. M. Rao, P. C. Eklund, Electrochemical oxidation of single wall carbon nanotube bundles in sulfuric acid. *J. Phys. Chem. B* **103**, 4292–4297 (1999).
20. P. Puech, T. Hu, A. Sapelkin, I. Gerber, V. Tishkova, E. Pavlenko, B. Levine, E. Flahaut, W. Bacsa, Charge transfer between carbon nanotubes and sulfuric acid as determined by Raman spectroscopy. *Phys. Rev. B.* **85**, 205412 (2012).
21. P. K. Rai, A. N. G. Parra-Vasquez, J. Chattopadhyay, R. A. Pinnick, F. Liang, A. K. Sadana, R. H. Hauge, W. E. Billups, M. Pasquali, Dispersions of functionalized single-walled carbon nanotubes in strong acids: Solubility and rheology. *J. Nanosci. Nanotechnol.* **7**, 3378–3385 (2007).
22. F. Mirri, A. W. K. Ma, T. T. Hsu, N. Behabtu, S. L. Eichmann, C. C. Young, D. E. Tsentalovich, M. Pasquali, High-performance carbon nanotube transparent conductive films by scalable dip coating. *ACS Nano* **6**, 9737–9744 (2012).
23. F. Mirri, N. D. Orloff, A. M. Forster, R. Ashkar, R. J. Headrick, E. A. Bengio, C. J. Long, A. Choi, Y. Luo, A. R. Hight Walker, P. Butler, K. B. Migler, M. Pasquali, Lightweight, flexible, high-performance carbon nanotube cables made by scalable flow coating. *ACS Appl. Mater. Interfaces* **8**, 4903–4910 (2016).
24. B. Dan, G. C. Irvin, M. Pasquali, Continuous and scalable fabrication of transparent conducting carbon nanotube films. *ACS Nano* **3**, 835–843 (2009).
25. L. Hu, D. S. Hecht, G. Grüner, Percolation in transparent and conducting carbon nanotube networks. *Nano Lett.* **4**, 2513–2517 (2004).
26. D. S. Hecht, A. M. Heintz, R. Lee, L. Hu, B. Moore, C. Cucksey, S. Risser, High conductivity transparent carbon nanotube films deposited from superacid. *Nanotechnology* **22**, 075201 (2011).
27. R. J. Headrick, D. E. Tsentalovich, J. Berdegué, E. A. Bengio, L. Liberman, O. Kleinerman, M. S. Lucas, Y. Talmon, M. Pasquali, Structure–property relations in carbon nanotube fibers by downscaling solution processing. *Adv. Mater.* **30**, 1704482 (2018).
28. S. Jiang, P.-X. Hou, M.-L. Chen, B.-W. Wang, D.-M. Sun, D.-M. Tang, Q. Jin, Q.-X. Guo, D.-D. Zhang, J.-H. Du, K.-P. Tai, J. Tan, E. I. Kauppinen, C. Liu, H.-M. Cheng, Ultrahigh-performance transparent conductive films of carbon-welded isolated single-wall carbon nanotubes. *Sci. Adv.* **4**, eaap9264 (2018).
29. S. Kim, J. Yim, X. Wang, D. D. C. Bradley, S. Lee, J. C. deMello, Spin- and spray-deposited single-walled carbon-nanotube electrodes for organic solar cells. *Adv. Funct. Mater.* **20**, 2310–2316 (2010).
30. S. Bae, S. J. Kim, D. Shin, J.-H. Ahn, B. H. Hong, Towards industrial applications of graphene electrodes. *Phys. Scr.* **2012**, 014024 (2012).
31. P. Mustonen, D. M. A. Mackenzie, H. Lipsanen, Review of fabrication methods of large-area transparent graphene electrodes for industry. *Front. Optoelectron.* **13**, 91–113 (2020).
32. C. Ladd, J.-H. So, J. Muth, M. D. Dickey, 3D printing of free standing liquid metal microstructures. *Adv. Mater.* **25**, 5081–5085 (2013).
33. J. Sha, Y. Li, R. Villegas Salvatierra, T. Wang, P. Dong, Y. Ji, S.-K. Lee, C. Zhang, J. Zhang, R. H. Smith, P. M. Ajayan, J. Lou, N. Zhao, J. M. Tour, Three-dimensional printed graphene foams. *ACS Nano* **11**, 6860–6867 (2017).
34. C.-P. Wong, H. Ohnuma, G. C. Berry, Properties of some rodlike polymers in solution. *Journal of Polymer Science: Polymer Symposia.* **65**, 173–192 (1978).
35. R. J. Headrick, M. A. Trafford, L. W. Taylor, O. S. Dewey, R. A. Wincheski, M. Pasquali, Electrical and acoustic vibroscopic measurements for determining carbon nanotube fiber linear density. *Carbon.* **144**, 417–422 (2019).
36. B. Wijnen, E. J. Hunt, G. C. Anzalone, J. M. Pearce, Open-source syringe pump library. *PLOS ONE.* **9**, e107216 (2014).
37. C. E. Owens, R. J. Headrick, S. M. Williams, A. J. Fike, M. Pasquali, G. H. McKinley, A. J. Hart, Substrate-versatile direct-write printing of carbon nanotube-based flexible conductors, circuits, and sensors. *Adv. Funct. Mater.* **31**, 2100245 (2021).

Acknowledgments

Funding: This work was supported by the Air Force Office of Scientific Research (AFOSR) grants FA9550-12-1-0035, FA9550-15-01-0370, and FA9550-18-1-0014 (M.P.); Robert A. Welch Foundation, C-1668 (M.P.); Department of Energy (DOE) awards DE-EE0007865 (Office of Energy Efficiency and Renewable Energy–Advanced Manufacturing Office) and DE-AR0001015 (Advanced Research Projects Agency–Energy) (M.P.); National Aeronautics and Space Administration (NASA) Space Technology Research Institute (STRI) for Ultra-Strong Composites by Computational Design (US-COMP) (grant number NNX17AJ32G) (M.P.); NASA Space Technology Research Fellowship (NSTRF14), grant number NNX14AL71H (R.J.H.); National Defense Science and Engineering Graduate Research Fellowship (NDSEG) (C.E.O.); Air Force Office of Scientific Research (AFOSR) grant FA9550-19-1-7045 (Y.T.); United States-Israel Binational Science Foundation grant 2016161 (Y.T.); and the cryo-EM was performed at the Technion Center for Electron Microscopy of Soft Matter, supported by the Technion Russell Berrie Nanotechnology Institute (RBNI). **Author contributions:** Conceptualization: R.J.H., S.M.W., and M.P. Investigation: R.J.H., S.M.W., C.E.O., L.W.T., O.S.D., C.J.G., L.L., and A.M.Y. Supervision: R.J.H., Y.T., B.M., G.H.M., A.J.H., and M.P. Writing—original draft: R.J.H. and S.M.W. Writing—review and editing: All authors. **Competing interests:** M.P. has a financial interest in DexMat Inc., a company commercializing carbon nanotube fibers and films. The authors declare that they have no other competing interests. **Data and materials availability:** All data needed to evaluate the conclusions in the paper are present in the paper and/or the Supplementary Materials.

Submitted 10 September 2021
Accepted 4 February 2022
Published 27 April 2022
10.1126/sciadv.abm3285

ScienceAdvances

Versatile acid solvents for pristine carbon nanotube assembly

Robert J. Headrick, Steven M. Williams, Crystal E. Owens, Lauren W. Taylor, Oliver S. Dewey, Cedric J. Ginestra, Lucy Liberman, Asia Matatyaho Yaakobi, Yeshayahu Talmon, Benji Maruyama, Gareth H. McKinley, A. John Hart, and Matteo Pasquali

Sci. Adv., **8** (17), eabm3285.
DOI: 10.1126/sciadv.abm3285

Science Advances (ISSN) is published by the American Association for the Advancement of Science. 1200 New York Avenue NW, Washington, DC 20005. The title *Science Advances* is a registered trademark of AAAS.